Simulation of a Low Enthalpy Ablator into a Hypersonic Boundary-Layer

Wesley Condren* Tobias Hermann† Matthew McGilvray‡
Oxford Thermofluids Institute, University of Oxford, Oxford, England OX2 0ES, United Kingdom

Understanding the behaviour of ablative materials is required for improved margins for TPS for spacecrafts. Low enthalpy ablators are used in place of more typical ablative materials when the high enthalpies required for their ablation can not be reached in ground testing. These materials simulate the highly coupled nature of the heat and mass transfer that occurs at the surface of an ablative heat shield during re-entry, through their ability to sublimate. As a result, the study of low enthalpy ablators can provide insight into the behaviour of ablative materials during hypersonic fight by isolating a handful of phenomena that occur and interact with one another at their surface. Predicting the material response prior to any experimental test is needed. The code CLEARR (Code for Low Enthalpy Ablator Recession Rate) is presented in this work and provides a low cost method of predicting low enthalpy ablator response. The code utilises empirical correlations to determine the energy and mass balances at the material's surface and time evolution of internal temperature distribution, discretised using a crank-Nicholson algorithm. Its functionality is showcased by modelling a cylindrical sample composed entirely of the low enthalpy ablator naphthalene subject to a wide range of hypersonic flow conditions. The evaluated rate of ablation of the material and ultimately the total mass injected into the boundary-layer over a range of test times including the nominal test time in a hypersonic facility are shown in addition to the effect of the varying flow properties on the material response.

I. Nomenclature

α	=	Thermal Diffusivity, $m^2 s^{-1}$
γ	=	Ratio of Specific Heats
ρ	=	Density, kgm^{-3}
C_M	=	Mass Transfer Coefficient
C_P	=	Pressure Coefficient
c_p	=	Specific Heat Capacity, $Jkg^{-1}K^{-1}$
F	=	Blowing Ratio
h	=	Specific Enthalpy, Jkg^{-1}
k	=	Thermal Conductivity, Wm^2K^{-1}
Le	=	Lewis Number
M	=	Mach Number
$\dot{m}$	=	Mass Flux, $kgm^{-2}s^{-1}$
M_r	=	Molecular Weight, $kgkmol^{-1}$
P	=	Pressure, bar
$\dot{q}$	=	Heat Flux, Wm^{-2}
r	=	Radius, m
R	=	Specific Gas Constant, $Jkg^{-1}K^{-1}$
St	=	Stanton Number
t	=	Time, s
T	=	Temperature, K

*DPhil Candidate, Department of Engineering Science, University of Oxford.
†Postdoctoral Research Assistant, Department of Engineering Science, University of Oxford
‡Professor, Department of Engineering Science, University of Oxford

u = speed, ms^{-1}

subscripts

∞ = Free Stream
eq = Equilibrium
r = Recovery
s = Solid
v = Vapour
w = Wall

II. Introduction

Spacecraft atmospheric entry is taxing on the vehicle due to the extremely high thermal loads it has to endure [1]. In order to avoid the vehicles' outer surface sustaining critical damage as a result of the incident thermal energy, which would endanger the crew, thermal protection systems (TPS) are a necessity in any hypersonic flight case the most common being comprised of ablative materials. Ablative heat shields protect the vehicle's outer surface with a layer of material which, under the extreme conditions of re-entry, moves through a series of thermo-chemical processes to ultimately absorb and transfer energy away from it [2]. The processes include pyrolysis, the thermal decomposition of the material into a porous char layer and gaseous products, the subsequent injection of these pyrolysis gases into the hypersonic boundary layer alongside the sublimation of the solid material, and a myriad of high-temperature non-equilibrium chemistry [3]. As a consequence, the surface of ablative heat shields facilitate a very complex mix of phenomena that occur simultaneously.

In order to improve the design of ablative TPS, improvements in understanding their behaviour during flight is needed. This generates the necessity to re-create the high enthalpies ablative heat shields experience during operation on the ground which, is typically done using arc jets [4], [5]. Although a flight accurate thermochemical environment is achieved, these facilities lack the ability to match the distribution of flow over a given model geometry during flight [6], [7]. To capture this aspect of the problem, tunnels that can operate comfortably at flight Reynolds numbers are required. However, these aerodynamic tunnels cannot match the high enthalpies necessary to trigger the ablative process in typical carbon-based ablative materials.

To enable fundamental research into ablative TPS in these wind tunnels, the more typical carbon-phenolic materials can be substituted for low enthalpy ablators namely, water ice, dry-ice, camphor and, naphthalene [8]. The use of these materials isolates the coupled heat and mass transfer or 'natural' ablation process of traditional ablative materials but at significantly lower enthalpies. This simplifies the problem of conducting experiments or building models of low enthalpy ablators compared to their high-enthalpy counter parts by removing the non equilibrium thermochemistry effects and the significance of radiative heating but maintain relevance to the original problem as a result of the sublimation processes through which cold ablation occurs. The sublimation of solid material accounts for a significant proportion of the mass lost in traditional ablatives [9] and therefore the study of low enthalpy ablators in hypersonic environments can provide valuable insights into ablative heat shield behaviour.

The development of using low enthalpy ablators to create a reduced-physics ablation problem to investigate flight relevant ablation phenomena has been of interest for many years. The early study by Charwat [10] investigated the generation of three dimensional roughness patterns on conical models made from either naphthalene and camphor at Mach 3. This work on shape change was extended to spherical blunted cones at Mach 5 by Baker [11] where numerical data was compared to experimental data. Furthermore the work conducted by Lipfert and Ginovese [12] showcased the ability to collect meaningful data on boundary layer parameters on an ablating surface opting for dry ice and camphor to bypass the enthalpy limitations of their facility. More recent efforts have been numerical, building complex models to simulate low enthalpy ablators in a hypersonic environment such the work presented by Bianchi and Turchi [13] and more recently still that by Zibitsker et al. [14] both with the main focus on shape change, which necessitates a fully coupled CFD and material response code.

This paper presents a finite difference material response code that simulates the transient behaviour of a low enthalpy ablator subject to hypersonic flow. The main goal is to determine the rate of recession and ultimately the amount of vapour that is injected into the free stream as a benchmark for for further experimental work into cold ablation. The numerical model is separated into three sections discussing the modelling of the hypersonic flow, the solid-gas interaction at the surface of the low enthalpy ablator and the in-depth energy transfer. The capabilities of the code are showcased for naphthalene subject to laminar Mach 6 flow over a cylinder.

III. Numerical Model

CLEARR segments the problem into three parts, flow, solid-gas interaction and then energy transfer within the solid. Figure.(1) outlines the transfer of information between each segment for a single time step. This section defines how each block calculates the necessary parameters

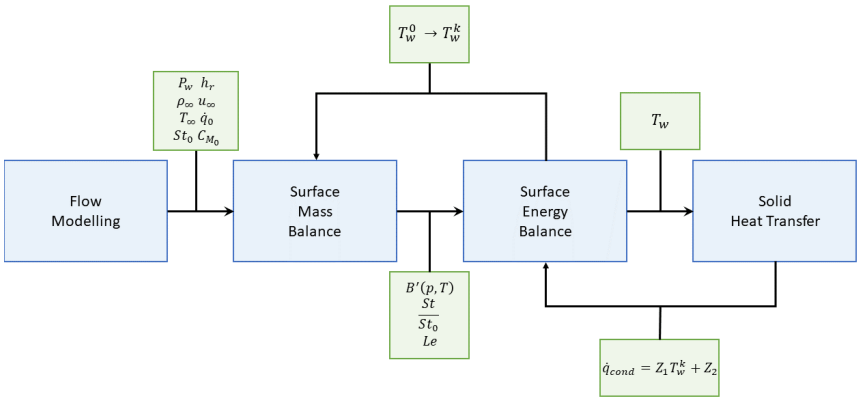

Fig. 1 Flow chart detailing internal processes of CLEARR and the interaction between each.

A. Flow Modelling

The necessary external flow parameters around the cylinder, due to the simple well studied geometry, are evaluated analytically from the total pressure, total temperature and, Mach number provided as inputs which saves a significant amount in computational cost in comparison to CFD codes. From the total free stream quantities, the undisturbed static pressure, temperature, density and flow velocity using isotropic relations. Following this, as the naphthalene sample is a blunt body, a strong normal shock will be present and as a result the incident flow will experience a drop in total pressure and an increase in static temperature over the shock, which are evaluated using Eq. (1) and Eq. (2) [15]

$$\frac{P_{0_2}}{P_\infty} = \left[\frac{(\gamma+1)^2 M_\infty^2}{4\gamma M_\infty^2 - 2(\gamma-1)}\right]^{\frac{\gamma}{\gamma-1}} \left[\frac{1-\gamma+2\gamma M_\infty^2}{\gamma+1}\right] \tag{1}$$

$$\frac{T_2}{T_\infty} = \frac{\left[1-\gamma+2\gamma M_\infty^2\right]\cdot\left[(\gamma-1)M^2+2\right]}{(\gamma+1)^2 M_\infty^2} \tag{2}$$

Where P_{0_2} is the post shock total pressure and T_2 is the post shock static temperature. The off stagnation point surface pressures are evaluated from the pressure coefficient distribution which is assumed to follow Newtonian Fluid theory's sine squared law shown in Eq. (3) [15].

$$C_P = \frac{P_w - P_\infty}{1/2\rho_\infty u_\infty^2} = C_{P_{max}} \cdot \sin^2\left(\frac{\pi}{2} - \phi\right) \tag{3}$$

Where ϕ is the angle around the cylinder surface ($\phi = 0$ refers to the stagnation point). $C_{P_{max}}$ is necessary to ensure the distribution reproduces the correct pitot pressure post shock from Eq. (1) and is as follows in Eq. (4).

$$C_{P_{max}} = \frac{P_{0_{shock}} - P_\infty}{1/2\rho_\infty u_\infty^2} \tag{4}$$

1. Convective Heat Transfer

The initial aero-thermal heating experienced at the stagnation point of the cylinder as a result of the incident hypersonic flow is evaluated using the Sutton-Graves correlation in Eq. (5) [16]. A hot wall correction is applied due to the low enthalpy of the flow being comparable to the wall enthalpy initially.

$$\dot{q}_{SG} = 1.7415 \cdot 10^{-4} \cdot \left(\frac{\rho_\infty}{R_n}\right)^{\frac{1}{2}} \cdot u_\infty^3 \cdot \left(1 - \frac{h_w}{h_\infty}\right) \tag{5}$$

Where R_n is the nose radius, h_w is the initial enthalpy at the wall and h_∞ is the free stream enthalpy.

The variation in the initial convective heating between $\phi = 0 - 90°$ is defined using the model developed by L.Lees in Ref.[17] for laminar flow over hemispherical blunt-nosed hypersonic vehicles. From this the initial or non-ablated Stanton number at each location on the cylinder surface is evaluated using Eq. (6)

$$St_0 = \frac{\dot{q}(\phi, 0)}{\rho_\infty u_\infty c_{p_\infty}(T_r - T_w)} \tag{6}$$

where $\dot{q}(0,0) = \dot{q}_{SG}$ and T_r is the recovery temperature defined by Eq. (7)

$$T_r = T_\infty \cdot \left[1 + r\left(\frac{\gamma + 1}{2}\right) \cdot M_\infty^2\right] \tag{7}$$

where r is the recovery factor which, for laminar flows is assumed to be equal to $\sqrt{Pr}$.

2. Blowing Heat Flux Augmentation

The cooling effect provided by the naphthalene vapour is described by defining first the blowing ratio F in Eq. (8).

$$F = \frac{\rho_v u_v}{\rho_\infty u_\infty} \tag{8}$$

Here the subscript v refers to the injected naphthalene vapour and thus numerator of Eq. (8) is simply mass flux evaluated from the surface mass balance. Normalising F by the non-ablated Stanton number defined in Eq. (6) defines the blowing paramater B_h shown in Eq. (9).

$$B_h = \frac{F}{St_0} \tag{9}$$

For a smooth flat surface subject to flow perpendicular to injection, the cooling effect experienced by the surface is of the following form.

$$\frac{St}{St_0} = \frac{\omega}{e^\omega - 1}, \quad \omega = B_h \cdot \left[\frac{M_{r_\infty}}{M_{r_v}}\right]^m \tag{10}$$

where ω is the blowing parameter augmented by the ratio of the molecular weight of the free stream to that of the injected gas. The exponent m, a fitting parameter to which the molecular weight ratio is raised, is taken to be 0.4 for laminar flow cases [18]. The reason for using the adjusted parameter is that, as molecular mass of the coolant is decreased, there is a greater volume of coolant injected into the boundary layer for the same mass flow rate. This results in a greater blockage effect, which is be captured by the empirical correction factor.

At a stagnation point the correlation in Eq. (10) no longer holds due to the presence of the normal shock, which it fails to account for. A different approach put forward first by Yoshikawa [19], takes into consideration the behaviour of gas inside the shock layer to derive the overall reduction experienced around the stagnation region shown in Eq. (11).

$$\frac{St}{St_0} = \left[\frac{L}{L_0}\lambda^{\frac{B_h}{B_*}}\right]^{-0.5} \frac{exp\left[\right] - \frac{1}{\pi}\frac{L}{L_0}\lambda^{\frac{B_h}{B}} B_h^2\Big]}{1 + erf\left[\frac{1}{\pi}\frac{L}{L_0}\lambda^{\frac{B_h}{B}}\right]^{0.5} B_h} \tag{11}$$

where B is the blowing parameter for boundary layer blow off defined as

$$B_* = 1.59 \cdot \sqrt{\frac{M_{r_v}}{28.9}} \tag{12}$$

$\frac{L}{L_0}$ is the ratio of shock stand-off for a transpiring surface to a non-transpiring surface defined for adiabatic flow over an axisymmetric body in Eq. (13) and λ is a correction parameter accounting for effects of the coolants molecular weight shown in Eq. (14) where $\bar{N}_v$ is a weighting factor which, for a polyatomic gas, is taken as 1 [20].

$$L/L0 = 1 + \sqrt{\frac{p_e}{p_\infty}\frac{M_{r_\infty}}{M_{r_v}}} St_0 B_h \tag{13}$$

$$\lambda = \sqrt{\frac{M_{r_\infty}}{M_{r_v}}} \cdot \bar{N}_v \tag{14}$$

For cylindrical geometry there is a lack of literature on correlations for blowing reduction distributions around the surface in a hypersonic flow field. As a result an assumption of a sine squared law is taken, which varies the observed blowing reduction from that calculated via Yoshikawa's relation in Eq. (11) at the stagnation point ($\phi = 0$) to that for a flat plate in Eq. (10) at $\phi = 90$degrees show in Eq. (15).

$$\frac{St}{St_0}(\phi) = \left[\frac{St}{St_0}\right]_{Flat} + \left(\left[\frac{St}{St_0}\right]_{Yosh} - \left[\frac{St}{St_0}\right]_{Flat}\right) \cdot sin^2\left(\frac{\pi}{2} - \phi\right) \tag{15}$$

B. Solid-Gas Interaction

As a result of the strongly coupled heat and mass transfer present at an ablating surface a more complex boundary condition in the form of a surface mass and energy balance is required to determine its state as the simulation propagates through time [21], [22].

1. Surface Mass Balance

In the more general environment of pure thermo-chemical ablation of an ablative TPS, Eq. (16) details the conservation of mass at the ablating surface for every species i present.

$$J_{w,i} + \dot{m}_i = \dot{m}_w \cdot y_{w,i} \tag{16}$$

where the first term on the left hand side. $J_{w,i}$ refers to the mass flux as a result of diffusion towards the surface, $\dot{m}_i$ is the chemical production of species i and, $\dot{m}_w \cdot y_{w,i}$ is the injection of species i into the boundary layer colloquially known as the blowing mass flux. The mass transfer via diffusion $J_{w,i}$ is evaluated using a transfer coefficient approach, where a transfer coefficient augments a driving potential. In this case, a mass transfer coefficient C_M is employed and the relevant 'driving potential' is the difference in mass fraction at the ablating surface to that at the boundary layer edge $\left(y_{w,i} - y_{e,i}\right)$ defining $J_{w,i}$ as shown in Eq. (17) [23].

$$J_{w,i} = C_M \left(y_{w,i} - y_{e,i}\right) = \rho_\infty u_\infty St_M \left(y_{w,i} - y_{e,i}\right) \tag{17}$$

Substituting Eq. (17) back into the general surface mass balance in Eq. (16) and then applying the simplification of a single ablating species n in a non reacting flow forms Eq. (18).

$$\rho_\infty u_\infty St_M \left(y_{w,n} - y_{e,n}\right) + \dot{m}_n = \dot{m}_n \cdot y_{w,n} \tag{18}$$

With the assumption of a free stream that initially contains non of the ablating species the non dimensional ablation mass flux $B^{'}$ can be evaluated from the mass fraction of species n at the wall shown in Eq. (19).

$$B^{'} = \frac{\dot{m}_n}{\rho_\infty u_\infty St_M} = \frac{y_{w,n}}{1 - y_{w,n}} \tag{19}$$

Under the assumption of thermochemical equilibrium the mass fraction of naphthalene, species n, can be evaluated from its equilibrium partial pressure P_{eq}. In this work an the integrated Clausius-Clapeyron equation assuming negligible solid specific volume relative to that of the naphthalene vapour is utilised shown in Eq. (20) and naphthalene's phase diagram defined by it is shown in Fig.(2) [24].

$$P_{eq}(T) = P_{ref} \cdot exp\left(\frac{h_{sub}}{R} \cdot \left(\frac{1}{T_{ref}} - \frac{1}{T}\right)\right) \tag{20}$$

Here T_{ref} and P_{ref} are a reference temperature and pressure taken to be the values at the triple point of naphthalene, 353K and 1000Pa respectively. The parameter h_{sub} is the sublimation enthalpy of the material, which is taken as

$0.572 MJkg^{-1}$ for naphthalene [25]. Furthermore, this sublimation enthalpy is assumed constant with temperature within the sublimation regime of naphthalene (at temperatures lower than 353K) [13].

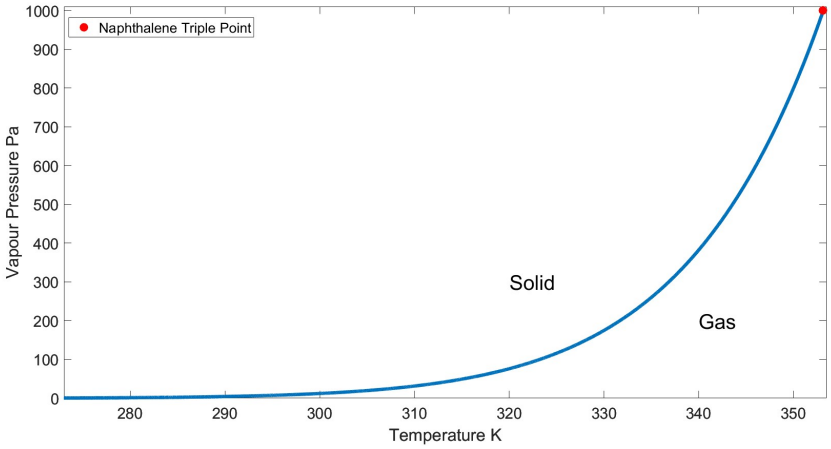

Fig. 2 Naphthalene Phase Diagram

The naphthalene mass fraction at the wall is then found through the relationship between it, naphthalene's mole fraction and partial pressure shown in Eq. (21).

$$y_{w,n} = x_n \cdot \frac{M_{r_n}}{\bar{M}_r} = \frac{P_{eq}}{P_w} \cdot \frac{M_{r_n}}{\bar{M}_r} \tag{21}$$

Where P_s is the local surface pressure evaluated from Eq.(3) and $\bar{M}_r$ is the average molecular weight of the mixture defined by Eq. (22)

$$\bar{M}_r = \Sigma_{i=1}^{N} x_i \cdot M_{r_i} \tag{22}$$

The free stream is assumed to be made of 79% nitrogen and 21% oxygen by volume (76.7% and 23.3 by mass) and that, as the flow is non reacting, molecular nitrogen and oxygen continue to exist in the same relative mole fractions at ablating wall. Combing Eqs (20)-(22) the non dimensional sublimation mass flux can then be evaluated for a given temperature and pressure as shown in Fig.(3).

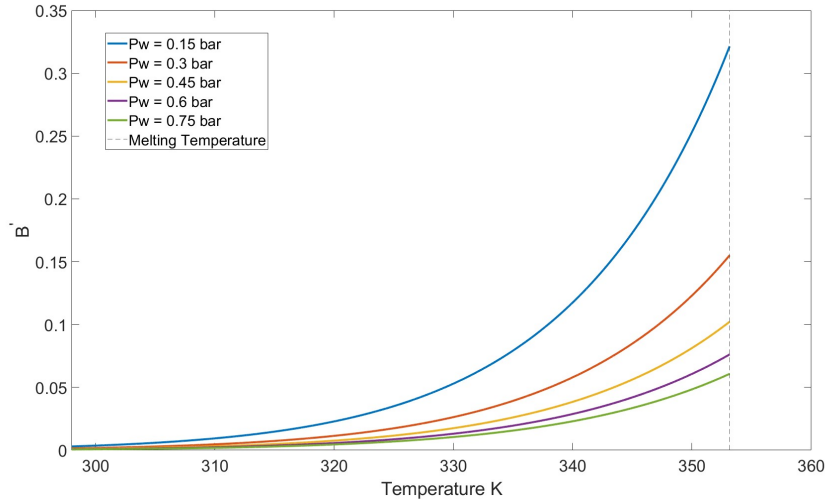

Fig. 3 Non-dimensional sublimation mass flux of naphthalene as a function of temperature and wall pressure.

The surface recession is then evaluated for a given sublimation mass flux by dividing through by the material's solid density highlighted in Eq. (23).

$$\dot{s} = \frac{C_M B'}{\rho_s} = \frac{\dot{m}_w}{\rho_s} \tag{23}$$

The mass transfer stanton number St_M and therefore the mass transfer coefficient C_M are evaluated by employing the Chilton-Colburn analogy to the concentration boundary layer which defines them as a function of the heat transfer Stanton number St shown in Eq. (24).

$$St_m = St \cdot Le^{\frac{2}{3}} \tag{24}$$

where St is evaluated as described in Section.3A.2 and Le is the Lewis number defined in Eq. (25).

$$Le = \frac{\alpha}{D_i} = \frac{k_w}{\rho_w c_{p_w} D} \tag{25}$$

Where D is the diffusion coefficient of naphthalene in air and k_w, ρ_w and c_{p_w} are the local conductivity, density and specific heat capacity of the naphthalene-air mixture at the wall respectively. The conductivity of the mixture is defined using Wilke's mixing rule (detailed in Appendix.A) and the mixture's density and specific heat capacity are taken as a weight average of the individual species quantities. The diffusivity, conductivity and viscosity of naphthalene are evaluated using polynomial fits as described by Yaws in Refs.[26], [27], [28] and shown in Eq. (26) - Eq. (28).

$$D = b_0 + b_1 \cdot T + b_2 \cdot T^2 \tag{26}$$

$$\mu = c_0 + c_1 \cdot T + c_2 \cdot T^2 + c_3 \cdot T^3 \tag{27}$$

$$k = d_0 + d_1 \cdot T + d_2 \cdot T^2 + d_3 \cdot T^3 \tag{28}$$

The constants of which are listed in Tables. 6-8 in Appendix.B. Finally, the specific heat capacity is evaluated using a NASA 7 polynomial shown in Eq. (29).

$$\frac{c_p}{R} = a_1 \cdot T^{-2} + a_2 \cdot T^{-1} + a_3 + a_4 \cdot T + a_5 \cdot T^2 + a_6 \cdot T^3 + a_7 \cdot T^4 \tag{29}$$

The constants a_1 - a_7 for naphthalene are listed in Table. 9. Similarly, for the free stream species NASA 7 polynomials were utilised and Sutherlands law shown in Eqs. (30) (31) were used to calculate their specific heat capacity, viscosity and conductivity.

$$\frac{\mu}{\mu_0} = \left(\frac{T}{T_0}\right)^{\frac{3}{2}} \cdot \frac{T_0 + S_\mu}{T + S_\mu} \tag{30}$$

$$\frac{k}{k_0} = \left(\frac{T}{T_0}\right)^{\frac{3}{2}} \cdot \frac{T_0 + S_k}{T + S_k} \tag{31}$$

Where μ_0 and k_0 are the viscosity and conductivity a the reference temperature T_0 of 273 K, S_μ and S_k are sutherland constants for viscosity and conductivity respectively. The constants and reference values for molecular nitrogen and oxygen are shown in Table.(1)

Table 1 Material properties of solid camphor

Gas	T_0	μ_0 [Pas]	S_μ [K]	k_0 [$\mathrm{Wm^{-1}K^{-1}}$]	S_k [K]
N_2	T_0	1.663e-5	107	0.0242	150
O_2	T_0	1.919e-5	139	0.0244	240

2. Surface Energy Balance

Taking a similar control volume as done to formulate Eq. (16) at the solid-gas interface and considering the energy terms feeding into or out of the volume, a surface energy balance for an ablative material can be defined. Figure. 4 shows the heat flux terms present at the wall for the general ablation problem leading to the construction of Eq. (32).

$$\dot{q}_{conv} + \dot{q}_{rad_{in}} + \dot{m}_w h_s + \dot{q}_{diff} = \dot{q}_{cond} + \dot{q}_{rad_{out}} + \dot{m}_w h_v \tag{32}$$

Where $\dot{q}_{conv}$ is the convective heat flux, $\dot{q}_{cond}$ is the conductive heat flux moving into the material, $\dot{q}_{rad}(in)$ and $\dot{q}_{rad}(out)$ refer to the radiative heat flux from the free stream and the heat flux re-radiated from the ablative surface respectively, $\dot{q}_{diff}$ and $\dot{m}_w h_v$ are the enthalpies carried into and away from the surface via the diffusion of species and blowing and, lastly the term $\dot{m}_w h_s$ represents the energy within the solid material 'moving' towards the surface as it recesses.

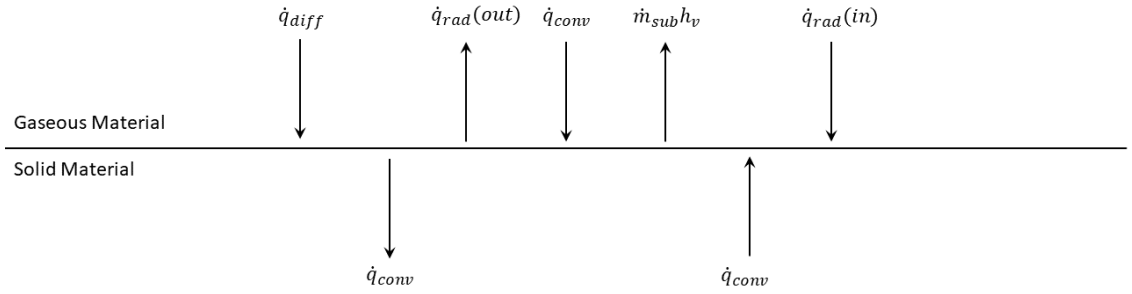

Fig. 4 Energy balance at the surface.

A simplification of Eq. (32) is achieved by neglecting the radiative heating input due to the significantly lower temperatures and then by multiplying the species surface mass balances by their respective enthalpies and summing over all species present shown in Eq. (33) and substituting this into the surface energy balance realising that $\sum_i J_{w,i} h_i$ is the total heat transferred via the diffusion of mass producing Eq. (34).

$$\sum_i J_{w,i} h_i + \sum_i \dot{m}_i h_i = \dot{m}_w h_w \tag{33}$$

$$\dot{q}_{conv} = \dot{q}_{cond} + \varepsilon\sigma \left(T_w^4 - T_\infty^4\right) + \left[\sum_i \dot{m}_i h_i - \dot{m}_w h_s\right] \tag{34}$$

$\sum_i \dot{m}_i h_i - \dot{m}_w h_s$ is the heat of reaction which, for the case of low enthalpy ablation, is reduced to the difference between the ablator's vapour enthalpy and that of its solid phase or more simply the sublimation enthalpy h_{sub} shown in Eq. (35).

$$\dot{q}_{conv} = \dot{q}_{cond} + \varepsilon\sigma \left(T_w^4 - T_\infty^4\right) + \dot{m}_w \cdot h_{sub} \tag{35}$$

The simplified surface energy balance is non linear with temperature and strongly coupled to the surface mass balance and therefore must be solved simultaneously using an iterative method.

C. Solid Heat Transfer

The energy transfer within the solid material is an essential part of ablation modelling [29], [30]. The equation that underpins the movement of energy through the solid in a highly transient environment with a recessing surface is shown in Eq. (36) [31].

$$\rho_s \frac{\partial h}{\partial t} = \frac{1}{A}\frac{\partial}{\partial r}\left(kA\frac{\partial T}{\partial r}\right) + \rho_s \dot{s}\frac{\partial h}{\partial r} \tag{36}$$

Where the terms from left to right are, the energy accumulation within the material, the net conduction through the solid and, the energy transferred as a result of the surface recessing at a rate $\dot{s}$. Note that this formulation assumes that conduction in the azimuthal direction is negligible compared to the flow of energy in the radial direction.

Assuming constant thermodynamic properties of the solid material in question and either rectangular,cylindrical or spherical polar symmetry Eq. (36) is reduced to Eq. (37).

$$\frac{\partial T}{\partial t} = \alpha \frac{1}{r^m} \frac{\partial}{\partial r} \left(r^m \frac{\partial T}{\partial r} \right) + \dot{s} \frac{\partial T}{\partial r} \tag{37}$$

Where the term α is the solid material's thermal diffusivity and the exponent m determines the coordinate system by setting it to a value of 0,1 or 2 for cartesian, cylindrical polars and spherical polars respectively.

IV. Discretisation of the Conduction Equation

A Crank-Nicholson's algorithm is employed to solve the adapted conduction equation Eq. (37). The method applies a central difference approximation to the time derivative with a step size of $\frac{1}{2}\Delta t$. As a result of this half time step, the arithmetic mean of the approximated spatial derivatives using the central difference method at the next and current time step is required in order to discretise the model in space. The end result, after applying the semi infinite boundary condition, is a system of $J-1$ equations shown in Eq. (38).

$$\begin{bmatrix} B_1 & C_1 & 0 & 0 & 0 & \dots & 0 \\ A_2 & B_2 & C_2 & 0 & 0 & \dots & 0 \\ 0 & A_3 & B_3 & C_3 & 0 & \dots & 0 \\ \vdots & & \ddots & \ddots & \ddots & & \vdots \\ 0 & & & \ddots & \ddots & \ddots & 0 \\ 0 & \dots & 0 & 0 & A_{J-2} & B_{J-2} & C_{J-2} \\ 0 & \dots & 0 & 0 & 0 & A_{J-1} & B_{J-1} \end{bmatrix} \begin{bmatrix} T_1^{n+1} \\ T_2^{n+1} \\ T_3^{n+1} \\ \vdots \\ T_{J-2}^{n+1} \\ T_{J-1}^{n+1} \end{bmatrix} = \begin{bmatrix} D_1 \\ D_2 \\ D_3 \\ \vdots \\ D_{J-2} \\ D_{J-1} \end{bmatrix} \tag{38}$$

Here A_j, B_j, C_j and D_j are the following functions of the time step Δt, the radial mesh spacing Δr, the recession rate $\dot{s}$, the material's thermal diffusivity α and the temperature value of the jth node at the nth time step T_j^n.

$$A_j = -\left(2\alpha\Delta t - m\frac{\alpha\Delta r\Delta t}{a - j\Delta r} - \dot{s}\Delta r\Delta t \right) \tag{39}$$

$$B_j = 4\Delta r^2 + 4\alpha\Delta t \tag{40}$$

$$C_j = -\left(2\alpha\Delta t + m\frac{\alpha\Delta r\Delta t}{a - j\Delta r} + \dot{s}\Delta r\Delta t \right) \tag{41}$$

$$D_j = -A_j T_{j-1}^n + (B_j - 8\alpha\Delta t) T_j^n - C_j T_{j+1}^n \tag{42}$$

The Jth equation is omitted from Eq. (38) as T_J, due to the semi infinite approximation at the centre, is known for all time steps and is therefore trivial. As for the surface node, the constants C_1 and D_1 take a different form as a result of the conductive heat flux ,$\dot{q}_{cond}$, present at the boundary shown in Eq. (43) and Eq. (44).

$$C_1 = -4\alpha\Delta t \tag{43}$$

$$D_1 = -\frac{2\Delta r}{k} A_1 \left(q_{cond}^n + q_{cond}^{n+1} \right) + (B_1 - 8\alpha\Delta t) \cdot T_1^n + 4\alpha\Delta t \cdot T_2^n \tag{44}$$

A. Coupling with the Surface Energy Balance

The surface energy balance requires a functional relationship between the surface wall temperature and the conductive heat flux $\dot{q}_{cond}$ in order to find a solution. This is obtained by coupling the energy balance at the surface to the internal energy balance described in Section.3B through the following simple algebraic manipulation of the system of equations summarised by the tri-diagonal matrix equation in Eq. (38).

$$A_{J-1} T_{J-2}^{n+1} + B_{J-1} T_{J-1}^{n+1} = D_{J-1} \tag{45}$$

$$A_{J-2}T_{J-3}^{n+1} + B_{J-2}T_{J-2}^{n+1} + C_{J-2}T_{J-1}^{n+1} = D_{J-2} \tag{46}$$

Extracting the final and penultimate node equations (shown in Eq. (45) and Eq. (46) respectively) then rearranging the last for T_{J-1}^{n+1} and substituting into the second to last constructs Eq. (47).

$$A_{J-2}T_{J-3}^{n+1} + \left(B_{J-2} - C_{J-2}\frac{A_{J-1}}{B_{J-1}}\right)T_{J-2}^{n+1} = D_{J-2} - C_{J-2}\frac{D_{j-1}}{B_{J-1}} \tag{47}$$

This process is repeated with the $J-3$ node and the altered form of the second to last equation Eq. (47) then the $J-4$ and the altered $J-3$ equation and so on, propagating the change through the entire system of equations, forming the reduced tri-diagonal matrix equation Eq. (48).

$$\begin{bmatrix} B_1^* & 0 & 0 & 0 & 0 & \dots & 0 \\ A_2^* & B_2^* & 0 & 0 & 0 & \dots & 0 \\ 0 & A_3^* & B_3^* & 0 & 0 & \dots & 0 \\ \vdots & & \ddots & \ddots & \ddots & & \vdots \\ 0 & & & \ddots & \ddots & \ddots & 0 \\ 0 & \dots & 0 & 0 & A_{J-2}^* & B_{J-2}^* & 0 \\ 0 & \dots & 0 & 0 & 0 & A_{J-1}^* & B_{J-1}^* \end{bmatrix} \begin{bmatrix} T_1^{n+1} \\ T_2^{n+1} \\ T_3^{n+1} \\ \vdots \\ T_{J-2}^{n+1} \\ T_{J-1}^{n+1} \end{bmatrix} = \begin{bmatrix} D_1^* \\ D_2^* \\ D_3^* \\ \vdots \\ D_{J-2}^* \\ D_{J-1}^* \end{bmatrix} \tag{48}$$

Where the constants A_j^*, B_j^*, C_j^* and, D_j^* are defined, for $j = 1$ to $J-1$, as

$$\begin{aligned} A_j^* &= A_j \\ B_j^* &= B_j - C_j\frac{A_{j+1}^*}{B_{j+1}^*} \\ D_j^* &= D_j - C_j\frac{D_{j+1}^*}{B_{j+1}^*} \end{aligned} \tag{49}$$

where as those for the final node, $j = J$ in the matrix equation, remain unchanged.

Finally, the relationship between the conductive heat flux and the wall temperature in Eq. (50) is found through the rearranging of first equation in Eq. (48), realising that D_1^* contains information about $\dot{q}_{cond}$ at the next and current time steps.

$$\dot{q}_{cond}^{n+1} = Z_1 \cdot T_1^{n+1} + Z_2 \tag{50}$$

Here T_1^{n+1} is the wall temperature and Z_1 and Z_2 are constants defined as follows

$$\begin{aligned} Z_1 &= -\frac{B_1^* k}{2\Delta r A_1} \\ Z_2 &= \frac{k}{2\Delta r A_1}\left[(4\Delta r^2 - 4\alpha\Delta t)T_1^n + 4\alpha\Delta r T_2^n\right] - \frac{kC_1}{2\Delta r A_1}\frac{D_1^*}{B_1^*} - \dot{q}_{cond}^n \end{aligned} \tag{51}$$

V. Numerical Procedure

The algorithm used to solve the coupled surface mass and energy balances is detailed below. At step 8 when the initial guess at the wall temperature is made the surface energy balance will equal some non zero value E. To produce a better estimate of the wall temperature that drives E closer to zero, newton-raphson iterative procedure is used where the next guess T_w^{k+1} is defined as shown in Eq. (52).

1) Set the free stream conditions P_0, T_0, M and cylinder radius a
2) Evaluate the initial heat flux, St_0 and, the surface pressure from C_p
3) Make an initial guess at the surface temperature T_w^0
4) Evaluate the equilibrium vapour pressure using Eq. (20)
5) Evaluate the dimensionless sublimation mass flux $B^{'}$ from Eq. (19)
6) Evaluate the local mixture density, specific heat capacity and conductivity
7) Calculate the local Lewis number with Eq. (25)
8) Construct the surface energy balance as laid out in
9) Iterate the wall temperature using the newton raphson method detailed in Eq. (52)
10) Repeat steps 4-9 until satisfactory convergence as been reached

$$T_w^{k+1} = T_w^k - E \cdot \left(\frac{\partial E}{\partial T}\right)^{-1} \tag{52}$$

When the iterative procedure has converged to a temperature value the surface recession $\dot{s}$ is then updated via Eq. (23). Furthermore, the solution defines the surface node temperature T_1^{n+1}. With this now known the second equation in the reduced system of equations Eq. (48) can be solved for T_2^{n+1} and then the third for T_3^{n+1} and so on continuing until all nodal temperature values at the next time step are known. This process is detailed for the jth node in Eq. (53).

$$T_j^{n+1} = \frac{D_j^*}{B_j^*} - \frac{A_j^*}{B_j^*} T_{j-1}^{n+1} \tag{53}$$

This then readies the system for the next time step.

VI. Validation Cases

In order to ensure the finite difference scheme is behaving correctly, standard heat transfer problems were run and checked against their analytical result.

A. Transient Semi-infinite Solid Exposed to Step in Surface Temperature

The transient behaviour of CLEARR was tested against the well known problem of a semi-infinite body exposed to a step in surface temperature. The initial condition was set to 293 K and the surface temperature was increased to 400 K at time $t = 0$. Figure. 5 shows the output of CLEARR and how it compares to the analytical solution for a exposure time of 0.5 s.

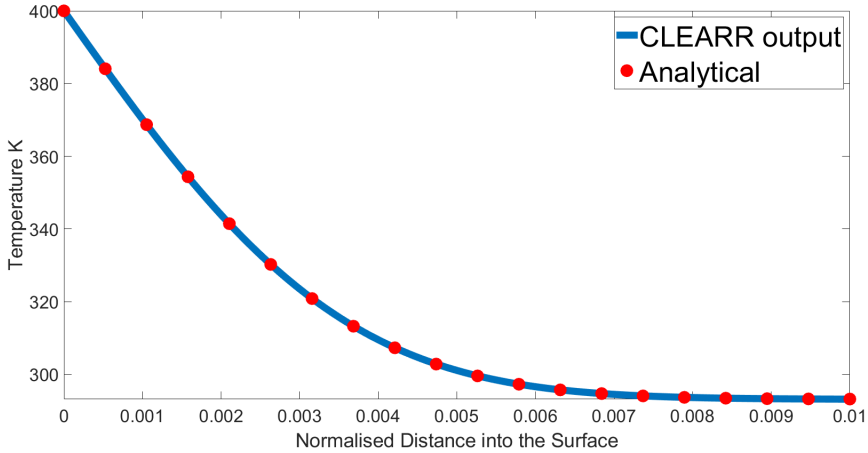

Fig. 5 Numerical temperature profiles of a transient semi-infinite body with a step from 293 K to 400 K compared to the analytical solution.

The output is in very good agreement with the exact solution and validates the use of the semi infinite approximation as the penetration depth is less than 1% of the cylinder radius.

B. Steady-Sate Semi-infinite Solid Exposed to Step in Surface Temperature

The same simulation that validated the transient response was allowed to run for a sufficiently large length of time such that any transient behaviour diminished, reaching a steady state. Figure. (6 shows the comparison to the exact solution, and again the numerical output is shown to be in good agreement with the exact solution.

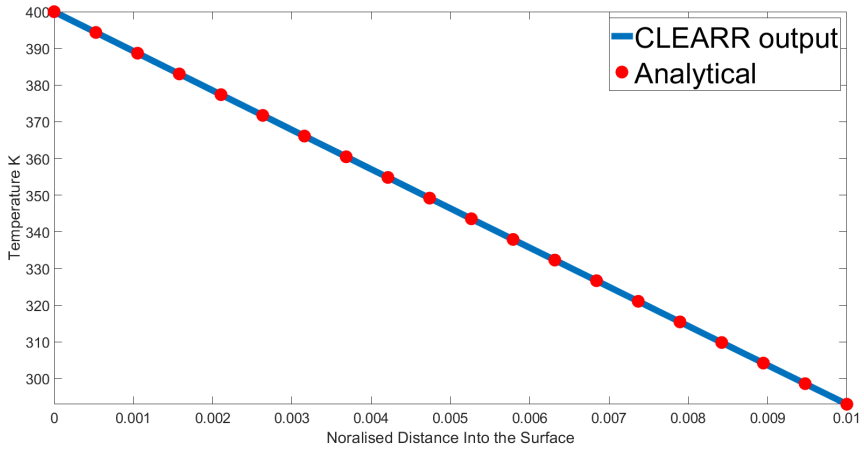

Fig. 6 Numerical steady-state temperature profile of semi-infinite bodywith a step from 293 K to 400 K compared to the analytical solution.

C. Validation of the Surface Mass and Energy Balances

The experimental work of Turchi et.al. [32] was used to compare to the output of a full simulation using CLEARR. In the work a scaled model of a Phoebus capsule with a 20 mm nose radius and a heat shield comprised of camphor was subject to three test conditions summarised in Table.2 for a total of 30s. The recession experienced by the stagnation point of the capsule was measured using photogrammetry in conjunction with side-on profile tracking with an average uncertainty of ±0.14mm. CLEARR simulated all three test cases using the total free stream conditions and Mach number as inputs with a 20 mm radius and spherical polar coordinate system for a total of 10s. Additionally, the material properties for camphor were evaluated using the same polynomial fits used for naphthalene as described in Section 3.B where the coefficients for camphor are as described in Tables.10 - 13. the material properites of the solid camphor are detailed in Table.3. It is important to note that after 6s of exposure the heat penetration depth equalled the thickness of the camphor layer and as a result the copper on which the low enthalpy ablator was fixed to began having an affect on the sublimation processes. As this copper substrate is not modelled in the current build of CLEARR the following comparisons are only made for the initial 6s of the test. Lastly, it is important to note that the experimental data does not start at time t=0 and so in order for comparisons to be drawn the data is shifted in time.

Table 2 Free stream conditions of the camphor phoebus capsule experiment [32]

Test	P_0 bar	T_0 K	M
$P15$	15.65	524.78	6
$P20$	20.57	487.2	6
$P25$	25.66	511	6

Table 3 Material properties of solid camphor

Property	Value
M_r	152.2 gmol^{-1}
ρ_s	990 kgm^{-3}
c_p	1781 $\text{Jkg}^{-1}\text{K}^{-1}$
k	0.2 $\text{W}m^{-1}\text{K}^{-1}$
ε	0.88

Figure.7 shows comparison between the experimentally acquired stagnation point recession and the data from CLEARR. It can be seen that the recession predicted by CLEARR agrees well with the experimental data set staying well within the experimental uncertainty for the entire 6s interval for all 3 test cases. Moreover, the lack of the heat sink effect due to the copper support material is highlighted as post 6s the experimentally obtained recession begins to decrease and move away from that predicted by CLEARR.

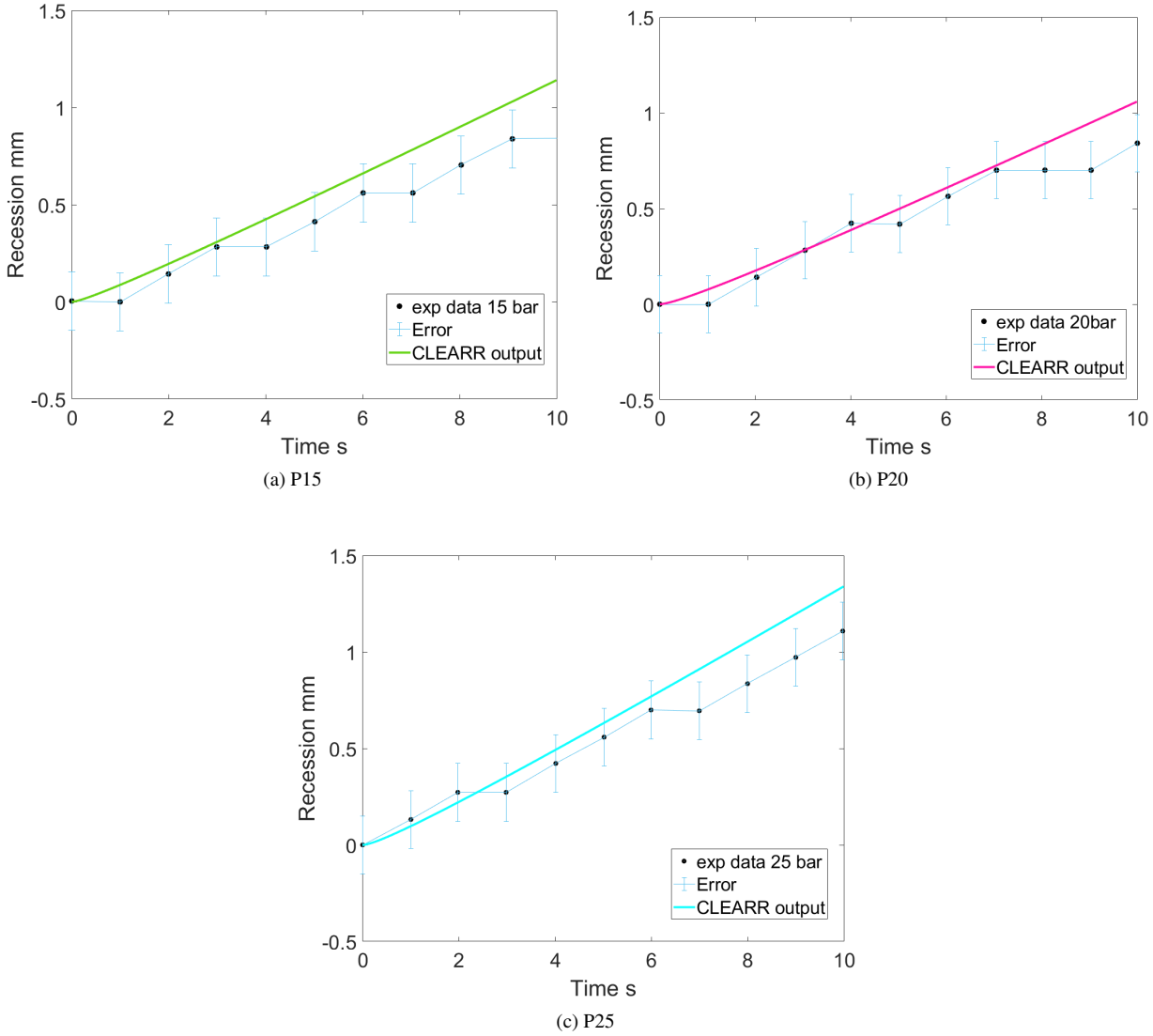

(a) P15

(b) P20

(c) P25

Fig. 7 Comparison of the stagnation point recession between numerical and experimental data.

VII. Results

This section details the simulation results of a 20 mm radius cylindrical sample of naphthalene subject to the hypersonic flow field summarised in Table.4 for a total of 10s and the material properties for the solid material are shown in Table.5. This condition was selected as a baseline as the total temperature and pressure are well within the operating envelope of many low enthalpy hypersonic facilities. The temperature and mass flux profiles around the circumference of the low enthalpy ablator at t = 0, 0.5,1,5,10 s are shown in addition to the radial temperature profiles and the temporal variation in recession and recession rate of 5 points alone the surface spaced by $\phi = 20°$ including the stagnation point. Additionally a study on the effect of free stream conditions on the predicted recession rate is also showcased.

Table 4 Free stream conditions for the base test case

Test	P_0 bar	T_0 K	M
Base Line	20	450	6

Table 5 Material properties of solid naphthalene

Property	Value
M_r	128.16 gmol^{-1}
ρ_s	1140 kgm^{-3}
c_p	1193 $\text{Jkg}^{-1}\text{K}^{-1}$
k	0.13 $\text{Wm}^{-1}\text{K}^{-1}$
ε	0.88

A. Base Condition Simulation

Figure.8 shows the temperature and sublimation mass flux profiles around the surface the naphthalene samples. As expected the temperature and sublimation mass flux around the surface both decrease from a maximum at the stagnation point to a minimum at $\phi = 80°$ as a result of diminishing energy input from the flow and the cooling effect of a given mass flux increasing due to a much lower surface pressure and therefore higher mass fraction of naphthalene. Furthermore the stagnation point temperature predicted is 348 K, 5 degrees lower than the melting temperature of naphthalene, and therefore narrowly avoiding surface melting considering the surface pressure at the stagnation point is significantly higher than naphthalene's triple point pressure of 1000Pa.

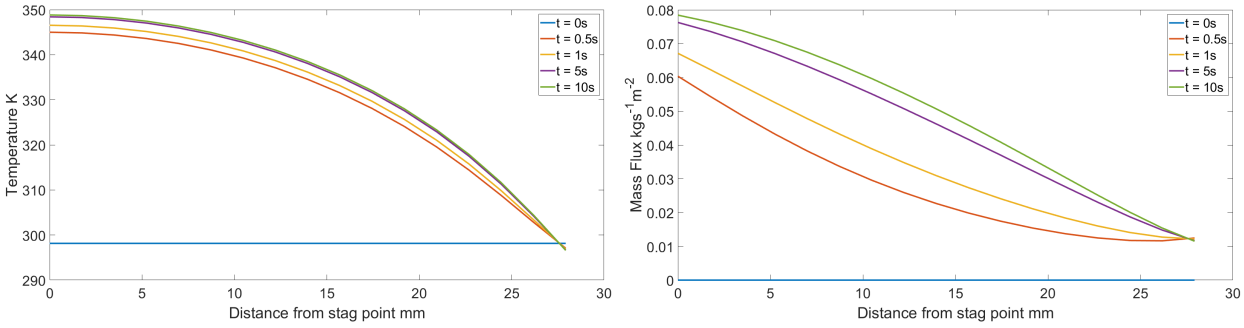

(a) Surface temperature

(b) Sublimation mass flux

Fig. 8 Surface profiles of the naphthalene sample's temperature and sublimation mass flux at the base line condition.

Fig.9a, Fig.9b and Fig.10 and detail the recession rate and recession and recessed shape respectively. The total recession predicted after 10s is little over 0.6mm, 3% of the initial radius, at the stagnation point which again diminishes

around the naphthalene surface. It is of note that the recession predicted is much lower than that achieved by camphor. This is primarily due to naphthalene having a significantly larger sublimation enthalpy and a higher density meaning more energy is required to gasify a smaller volume of material than camphor.

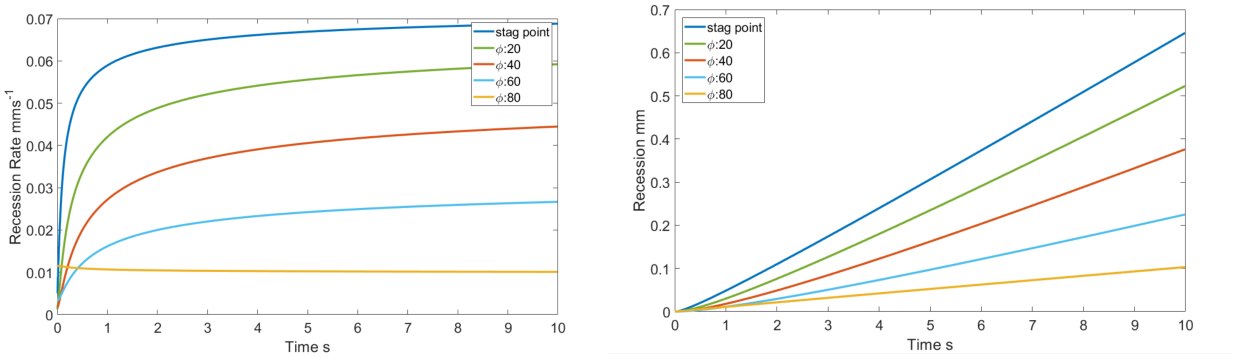

(a) Recession rate

(b) Total recession

Fig. 9 Temporal evolution of the total surface recession and recession rate at the base line condition.

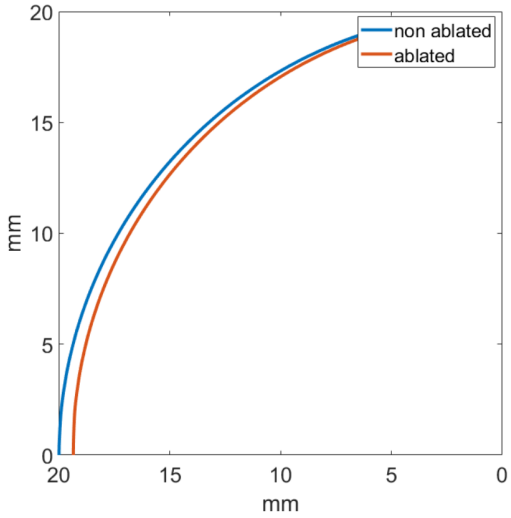

Fig. 10 Recessed shape of the naphthalene sample after 10s of exposure.

Lastly, the radial temperature profiles at the stagnation point and 20°,60° and 80° around the cylinder are shown in Fig.11. It can be seen that the penetration depth at the stagnation point is around 3.5mm after 10s of exposure which is an important parameter to note for any future experimental work when selecting initial low enthalpy ablator thickness.

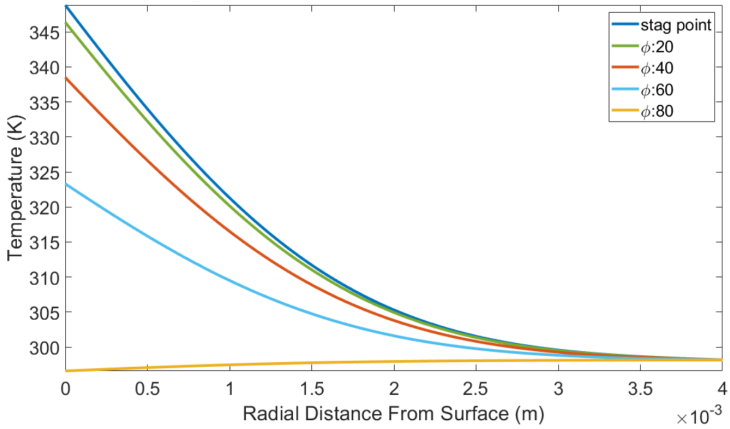

Fig. 11 Radial temperature profiles of the solid naphthalene sample.

B. Effect of Free Stream Conditions

A study into the effect of free stream conditions on the response of naphthalene was conducted in which the free stream total temperature and pressure were varied from 350-500K and 8-20bar respectively for both Mach 6 and 7 flow. The cylinder was exposed to the flow in each condition for a total of 10s and the surface temperature and total surface recession at the stagnation point were recorded shown in Fig.12 and Fig.13. It can be seen that for a given Mach number increasing the total temperature and pressure results in a higher surface temperature and surface recession the latter being to a less significant degree than the prior. This primarily due to the increase in initial convective heat transfer as a result of a more dense flow with higher total pressure and a faster moving flow with increasing total temperature.

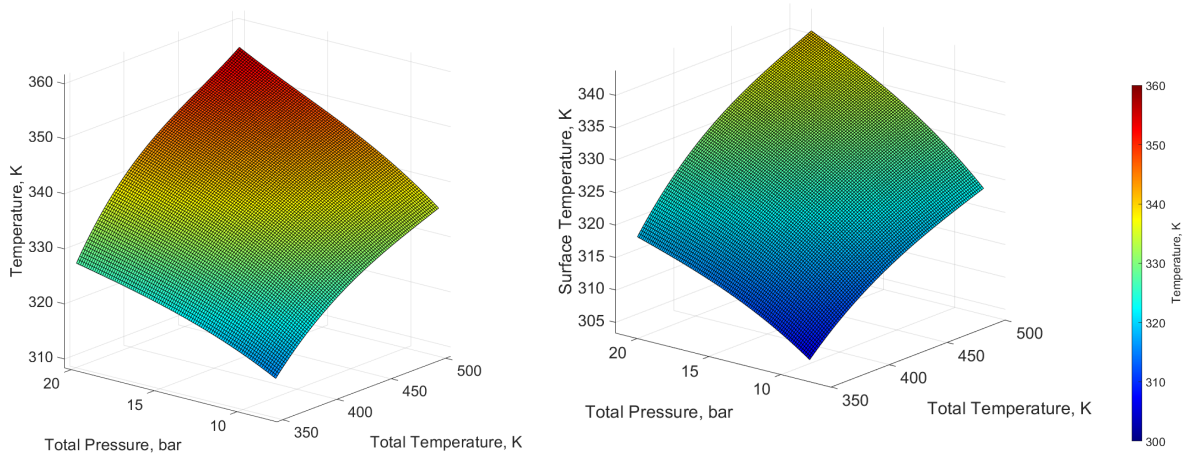

(a) Mach 6 (b) Mach 7

Fig. 12 Variation of stagnation point surface temperature after 10s of exposure with free stream total temperature and pressure.

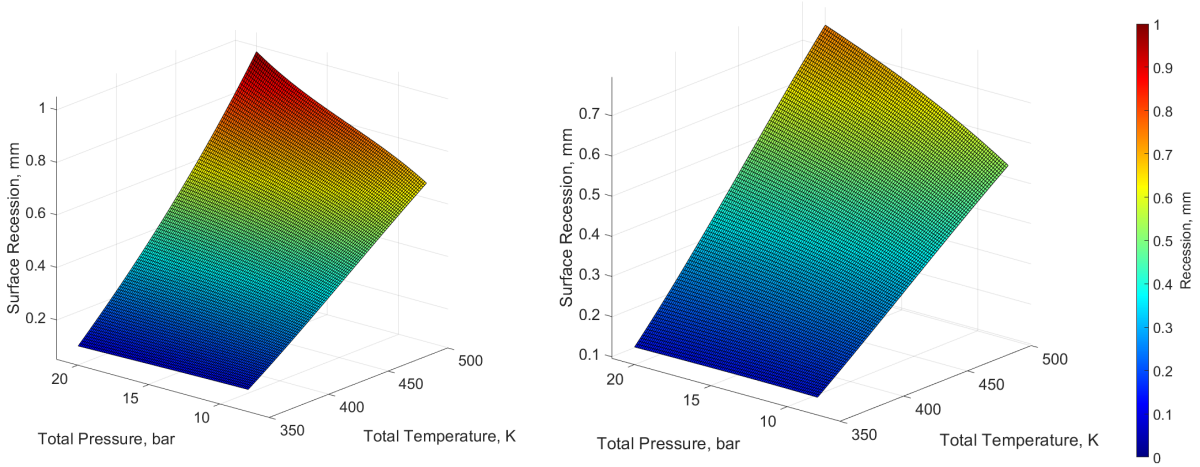

(a) Mach 6

(b) Mach 7

Fig. 13 Variation of stagnation point surface recession after 10s of exposure with free stream total temperature and pressure.

The effect of free stream Mach number is showcased when comparing the stagnation point temperature plots for Mach 6 and 7. At Mach 6 the stagnation point temperature for every condition is greater than that at achieved at Mach 7. This is a consequence of the free stream mass flux diminishing as Mach number increases which in turn drives the blowing parameter B_h up for a given sublimation mass flux. Therefore, cooling the solid naphthalene surface to a greater degree resulting in less sublimation which is highlighted in the lower stagnation point recession observed at Mach 7.

Lastly, between total pressures of 18 and 20 bar at Mach 6, total temperatures above 480 K pushed the stagnation point temperature above the melting point of naphthalene. As the triple point pressure of the material at these pressures is greatly exceeded, surface melting maybe observed during an experiment at these conditions. As the Mach number decreases the range of allowable conditions, those which avoid surface melting, similarly diminishes and vice versa - exhibited by the Mach 7 surface temperature being below the melting point for every condition.

VIII. Conclusion

To conclude, a finite difference code has been developed to simulate the response the low enthalpy ablator naphthalene subjected to hypersonic flow. The code was validated against the experiments performed Turchi et.al. showing good agreement prior to the copper heat sink effect. Moreover, it was shown that naphthalene is more shape stable than camphor, experiencing less surface recession for a given condition as a result of a higher density and sublimation enthalpy. This combined with the fact that diagnostic techniques like PLIF can take advantage of naphthalene's ability to fluoresce presents naphthalene as an excellent option to study the ablation effects and the transport of ablation products in hypersonic flows. Additionally, due to the low triple point pressure of the material at 1000 Pa, surface melting is possible when the melting temperature is exceeded which limits the available conditions that naphthalene can be subject to. This limitation was found to reduce at higher Mach numbers due to the increase in cooling effect provided by the sublimation process. Therefore greater total temperatures and pressures can be investigated at higher Mach numbers. Overall, the code provides a solid foundation on which to progress the study of ablative thermal protection systems.

Appendix

A: wilke's mixing rule

Wilke's mixing rule defines the conducitivity of a mixture as in Eq. (54) [33].

$$k = \Sigma_i^N \frac{x_i k_i}{\phi_i} \tag{54}$$

Where N is the total number of gases present in the mixture and ϕ_i is defined by Eq. (55)

$$\phi_i = \Sigma_j^N x_j \cdot \frac{\left[1 + \sqrt{\frac{\mu_i}{\mu_j}} \cdot \left(\frac{M_{r_j}}{M_{r_i}}\right)^{\frac{1}{4}}\right]^2}{\sqrt{8\left(1 + \frac{M_{r_i}}{M_{r_j}}\right)}} \tag{55}$$

B:Coefficients for Polynomial Fits

Table 6 Yaws coefficients for naphthalene in air diffusion coefficient $[cm^2s^{-1}]$ $200K \leq T \leq 1500K$ **[26]**

	b_0	b_1	b_2
Value	-4.311e-2	2.5699e-4	4.1853e-7

Table 7 Yaws coefficients for the viscosity of naphthalene $[Pas \times 10^{-7}]$ $275K \leq T \leq 1500K$ **[28]**

	c_0	c_1	c_2	c_3
Value	-16.611	2.5296e-1	-3.3558e-5	-1.0129e-9

Table 8 Yaws coefficients for the conductivity of naphthalene $[Wm^{-1}K^{-1}]$ $250K \leq T \leq 1500K$ **[27]**

	d_0	d_1	d_2	d_3
Value	-6.4056e-3	2.0372e-5	8.1863e-8	-2.9543e-11

Table 9 NASA Glenn coefficients for calculating naphthalene's specific heat capacity $200K \leq T \leq 1000K$ **[34]**

Coefficient	Value
a_1	-2.602845316e-5
a_2	6.237409570e3
a_3	-5.226095040e1
a_4	2.397692776e-1
a_5	-2.912244803e-4
a_6	1.854944401e-7
a_7	-4.816619270e-11

Table 10 Yaws coefficients for camphor in air diffusion coefficient $[cm^2s^{-1}]$ $200K \leq T \leq 1500K$ **[26]**

	b_0	b_1	b_2
Value	-8.157e-2	4.0775e-4	2.5260e-7

Table 11 Yaws coefficients for the viscosity of camphor $[Pas \times 10^{-7}]$ $275K \leq T \leq 1500K$ **[28]**

	c_0	c_1	c_2	c_3
Value	-0.7439	2.0215e-1	1.2145e-5	-1.5620e-8

Table 12 Yaws coefficients for the conductivity of camphor $[Wm^{-1}K^{-1}]$ $250K \leq T \leq 1500K$ **[27]**

	d_0	d_1	d_2	d_3
Value	-4.3828e-3	1.0500e-5	1.3260e-7	-4.9499e-11

Table 13 NASA Glenn coefficients for calculating camphor's specific heat capacity $200K \leq T \leq 1000K$ **[32]**

Coefficient	Value
a_1	0
a_2	0
a_3	-16.31699076
a_4	1.436655633e-1
a_5	-7.438199500e-5
a_6	0
a_7	0

References

[1] Turchi, A., Paris, S., Agostinelli, W., Grigat, F., Löhle, S., Bianchi, D., and Ferracina, L., "Assessment of the effect of heat-shield ablation on the aerodynamic performance of re-entry capsules in hypersonic flows," 2019.

[2] Panerai, F., Ferguson, J., Lachaud, J., Martin, A., Gasch, M., and Mansour, N., "Analysis of carbon fiber felts for flexible ablators using synchrotron hard x-ray micro-tomography," 2015. https://doi.org/10.13140/RG.2.1.2661.0084.

[3] Smits, L., Martin, P., and Girimaji, S., *Current Status of Basic Research in Hypersonic Turbulence*, AIAA, 2009. https://doi.org/10.2514/6.2009-151, URL https://arc.aiaa.org/doi/abs/10.2514/6.2009-151.

[4] Gokcen, T., Chen, Y.-K., Skokova, K. A., and Milos, F. S., "Computational Analysis of Arc-Jet Stagnation Tests Including Ablation and Shape Change," *Journal of Thermophysics and Heat Transfer*, Vol. 24, No. 4, 2010, pp. 694–707. https://doi.org/10.2514/1.46199, URL https://doi.org/10.2514/1.46199.

[5] Helber, B., Turchi, A., Scoggins, J. B., Hubin, A., and Magin, T. E., "Experimental investigation of ablation and pyrolysis processes of carbon-phenolic ablators in atmospheric entry plasmas," *International Journal of Heat and Mass Transfer*, Vol. 100, 2016, pp. 810–824. https://doi.org/https://doi.org/10.1016/j.ijheatmasstransfer.2016.04.072, URL https://www.sciencedirect.com/science/article/pii/S0017931015310243.

[6] Turchi, A., Saiz, J. J. M., Magin, T. E., and Chazot, O., "Duplication of Hypersonic Stagnation-Region Aerothermochemistry and Gas-Surface Interaction in High-Enthalpy Ground Testing," *Exp Fluids*, Vol. 62, No. 238, 2021. https://doi.org/https://doi.org/10.1007/s00348-021-03320-6.

[7] Rotondi, M., Migliorino, M. T., Bianchi, D., Pagani, P., and Turchi, A., "Numerical Assessment of Camphor Ablation Flight Relevance in Hypersonic Wind-Tunnel Testing," *Journal of Spacecraft and Rockets*, Vol. 59, No. 5, 2022, pp. 1574–1591. https://doi.org/10.2514/1.A35318, URL https://doi.org/10.2514/1.A35318.

[8] Kohlman, D. L., and Richardson, R. W., "Experiments on the use of dry ice ablating wind-tunnel models." *Journal of Spacecraft and Rockets*, Vol. 6, 1969, pp. 1061–1063.

[9] A.Turchi, e. a., "Assessment of the Effect of Heat-Shield Ablation on the Aerodynamic Performance of Re-Entry Capsules in Hypersonic Flows," *European Conference for Aeronautics and Aerospace Sciences*, 2019, p. 15 pages. https://doi.org/10.13009/EUCASS2019-608.

[10] Charwat, A. F., *Exploratory Studies on the Sublimation of Slender Camphor and Naphthalene Models in a Supersonic Wind-Tunnel*, RAND Corporation, Santa Monica, CA, 1968.

[11] Baker, R., *Low temperature ablator nosetip shape change at angle of attack*, AIAA, 1972. https://doi.org/10.2514/6.1972-90, URL https://arc.aiaa.org/doi/abs/10.2514/6.1972-90.

[12] Genovese, J., and Lipfert, F., *An experimental study of the boundary layers on low temperature subliming ablators*, AIAA, 1969. https://doi.org/10.2514/6.1969-152, URL https://arc.aiaa.org/doi/abs/10.2514/6.1969-152.

[13] D.Bianchi, and A.Turchi, "Numerical Analysis on the Sublimation of Low-Temperature Ablator Models Undergoing Shapes Changes in a Supersonic Wind-Tunnel," *European Conference for Aeronautics and Aerospace Sciences*, 2019. https://doi.org/10.13009/EUCASS2019-800.

[14] Zibitsker, A. L., McQuaid, J., Brehm, C., and Martin, A., *Fully-Coupled Simulation of Low Temperature Ablator and Hypersonic Flow Solver*, AIAA, 2022. https://doi.org/10.2514/6.2022-0676, URL https://arc.aiaa.org/doi/abs/10.2514/6.2022-0676.

[15] J.D.Anderson, *Hypersonic and High Temperature Gas Dynamics*, 2nd ed., AIAA, 1801 Alexander Bell Drive, Reston, Virginia, 1983, Chap. 3.

[16] K.Sutton, and R.A.Graves.Jr., "A General Stagnation-Point Convectibe-Heating equation for Arbitrary Gas Mixtures," *Nasa Techincal Report*, November 1971.

[17] L.Lees, "Laminar Heat Transfer Over Blunt-Nosed Bodies at Hypersonic Flight Speeds," *Journal of Jet Propulsion*, Vol. 26, No. 4, 1956, pp. 259–269. https://doi.org/10.2514/8.6977.

[18] Naved, I., Hermann, T., Hambidge, C., Saad Ifti, H., Falsetti, C., McGilvray, M., Tirichenko, I. S., and Vandeperre, L., "Transpiration-Cooling Heat Transfer Experiments in Laminar and Turbulent Hypersonic Flows," *Journal of Thermophysics and Heat Transfer*, Vol. 37, No. 2, 2023, pp. 281–295. https://doi.org/10.2514/1.T6626, URL https://doi.org/10.2514/1.T6626.

[19] Yoshikawa, K. K., "Linearized Theory of Stagnation Point Heat and Mass Transfer at Hypersonic Speeds," 1969.

[20] Tauber, M. E., "A review of high-speed, convective, heat-transfer computation methods," 1989.

[21] M.E.Ewing, T.S.Laker, and D.T.Walker, "Numerical Modelling of Ablation heat Transfer," *Journal of Thermophysics and Heat Transfer*, Vol. 27, No. 4, Oct 2013, pp. 615–632. https://doi.org/10.2514/1.T4164.

[22] Amar, A. J., Blackwell, B. F., and Edwards, J. R., "One-Dimensional Ablation Using a Full Newton's Method and Finite Control Volume Procedure," *Journal of Thermophysics and Heat Transfer*, Vol. 22, No. 1, 2008, pp. 71–82. https://doi.org/10.2514/1.29610, URL https://doi.org/10.2514/1.29610.

[23] D.Bianchi, "Modeling of Ablation Phenomena in Space Applications," Ph.D. thesis, Spaienza University of Rome, 2006.

[24] Cengel, Y., and Boles, M., *Thermodynamics: An Engineering Approach McGraw-Hill*, AIAA, New York, 2002.

[25] "National Institue of Standards and Tecnology Chemistry WebBook: Naphthalene," , Accessed 01-2022. URL https://webbook.nist.gov/cgi/cbook.cgi?ID=C91203&Mask=4.

[26] Yaws, C. L., "Chapter 10 - Diffusion Coefficient in Air – Organic Compounds," *Transport Properties of Chemicals and Hydrocarbons*, edited by C. L. Yaws, William Andrew Publishing, Boston, 2009, pp. 407–496. https://doi.org/https://doi.org/10.1016/B978-0-8155-2039-9.50015-6, URL https://www.sciencedirect.com/science/article/pii/B9780815520399500156.

[27] Yaws, C. L., "Chapter 5 - Thermal Conductivity of Gas – Organic Compounds," *Transport Properties of Chemicals and Hydrocarbons*, edited by C. L. Yaws, William Andrew Publishing, Boston, 2009, pp. 201–291. https://doi.org/https://doi.org/10.1016/B978-0-8155-2039-9.50015-6, URL https://www.sciencedirect.com/science/article/pii/B9780815520399500156.

[28] Yaws, C. L., "Chapter 1 - Viscosity of Gas – Organic Compounds," *Transport Properties of Chemicals and Hydrocarbons*, edited by C. L. Yaws, William Andrew Publishing, Boston, 2009, pp. 1–92. https://doi.org/https://doi.org/10.1016/B978-0-8155-2039-9.50015-6, URL https://www.sciencedirect.com/science/article/pii/B9780815520399500156.

[29] Kuo, K. K., and Keswani, S. T., "A Comprehensive Theoretical Model for Carbon-Carbon Composite Nozzle Recession," *Combustion Science and Technology*, Vol. 42, No. 3-4, 1985, pp. 145–164. https://doi.org/10.1080/00102208508960374, URL https://doi.org/10.1080/00102208508960374.

[30] Acharya, R., and Kuo, K. K., "Effect of Chamber Pressure and Propellant Composition on Erosion Rate of Graphite Rocket Nozzle," *Journal of Propulsion and Power*, Vol. 23, No. 6, 2007, pp. 1242–1254. https://doi.org/10.2514/1.24011, URL https://doi.org/10.2514/1.24011.

[31] D.Bianchi, F.Nasuti, and E.Martelli, "Coupled Analysis of Flow and Surface Ablation in Carbon-Carbon Rocket Nozzles," *Journal of Spacecraft and Rockets*, Vol. 46, No. 3, May 2009, pp. 492–500. https://doi.org/10.2514/1.40197.

[32] Rotondi, M., Migliorino, M. T., Bianchi, D., Pagani, P., and Turchi, A., "Numerical Assessment of Camphor Ablation Flight Relevance in Hypersonic Wind-Tunnel Testing," *Journal of Spacecraft and Rockets*, Vol. 59, No. 5, 2022, pp. 1574–1591. https://doi.org/10.2514/1.A35318, URL https://doi.org/10.2514/1.A35318.

[33] Wilke, C., "A viscosity equation for gas mixtures," *The Journal of chemical physics*, Vol. 18, No. 4, 1950, pp. 517–519.

[34] McBride, B., Zehe, M., and Gordon, S., "NASA Glenn coefficients for calculating thermodynamic properties of individual species," 2002.